Probing the Anisotropic Distortion of Photoexcited Spin Crossover Complexes with Picosecond X-ray Absorption Spectroscopy

14 AUTHORS, INCLUDING:

Sophie E. Canton

106 PUBLICATIONS   671 CITATIONS

SEE PROFILE

G. Jennings

Argonne National Laboratory

103 PUBLICATIONS   3,127 CITATIONS

SEE PROFILE

Charles A. Kurtz

Argonne National Laboratory

50 PUBLICATIONS   903 CITATIONS

SEE PROFILE

David Gosztola

Argonne National Laboratory

130 PUBLICATIONS   4,684 CITATIONS

SEE PROFILE

Probing the Anisotropic Distortion of Photoexcited Spin Crossover Complexes with Picosecond X-ray Absorption Spectroscopy

Sophie E. Canton,*,[†] Xiaoyi Zhang,*,[∥] Latévi M. Lawson Daku,[▽] Amanda L. Smeigh,[△] Jianxin Zhang,[‡] Yizhu Liu,[‡] Carl-Johan Wallentin,[‡] Klaus Attenkofer,[¶] Guy Jennings,[∥] Charles A. Kurtz,[∥] David Gosztola,[⊥] Kenneth Wärnmark,[‡] Andreas Hauser,[▽] and Villy Sundström*,[§]

[†]Department of Synchrotron Radiation Instrumentation, [‡]Centre for Analysis and Synthesis, Department of Chemistry, and [§]Department of Chemical Physics, Lund University, Box 124, 22100 Lund, Sweden

[∥]X-ray Sciences Division, and [⊥]Center for Nanoscale Materials, Argonne National Laboratory, 9700 South Cass Avenue, Argonne, Illinois 60439, United States

[▽]Département de Chimie Physique, Université de Genève, Quai E. Ansermet 30, CH-1211 Genève 4, Switzerland

[△]Department of Chemistry, Northwestern University, 2145 Sheridan Road, Evanston, Illinois 60208-3113, United States

[¶]Photon Science Directorate, Brookhaven National Laboratory, Upton, New York 11973-5000, United States

Ⓢ *Supporting Information*

ABSTRACT: For numerous spin crossover complexes, the anisotropic distortion of the first coordination shell around the transition metal center governs the dynamics of the high-spin/low-spin interconversion. However, this structural parameter remains elusive for samples that cannot be investigated with crystallography. The present work demonstrates how picosecond X-ray absorption spectroscopy is able to capture this specific deformation in the photoinduced high-spin state of solvated $[Fe(terpy)_2]^{2+}$, a complex which belongs to the prominent family of spin crossover building blocks with nonequivalent metal−ligand bonds. The correlated changes in Fe−N_{Axial}, Fe−N_{Distal}, and bite angle N_{Distal}−Fe−N_{Axial} extracted from the measurements are in very good agreement with those predicted by DFT calculations in D_{2d} symmetry. The outlined methodology is generally applicable to the characterization of ultrafast nuclear rearrangements around metal centers in photoactive molecular complexes and nanomaterials, including those that do not display long-range order.

$[Fe(terpy)_2]^{2+}$

X-ray probe

Optical pump
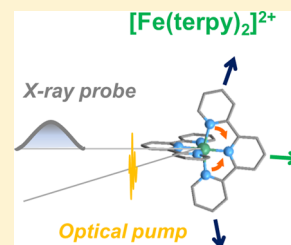
INTRODUCTION

When investigated at the molecular level, functionality is often related to a bistability induced by the interconversion between two states with distinct physicochemical properties. Discovered in the 1930s through the unexpected temperature-dependent magnetism of Fe^{III} dithiocarbamate derivatives,[1] the thermal equilibrium between the low-spin (LS) and the high-spin (HS) states of d^4−d^7 transition metal complexes, nowadays known as spin crossover (SCO), is a fundamental display of bistability widely encountered in material science, chemistry, and biology.[2] Functionalization based on this process requires manipulating selectively one of the two spin-states; therefore, controlling the dynamics of their interconversion is essential.[3,4] Following breakthrough experiments establishing that SCO can be impulsively triggered by Raman laser temperature jump, ultrasonic absorption, or light excitation,[5−7] decisive advances have been made in the identification of the key factors that govern the unimolecular rates.[8] The ligand-field splitting energy and the average metal−ligand (M−L) bond length R_{Av} are two such parameters. They correlate energetics and structure in the theoretical treatments of SCO as a nonadiabatic radiationless multiphonon process in the strong coupling limit.[9] From recent observations, there is increasing evidence that the anisotropic distortion of the first coordination shell (FCS) plays a determining role as well.[10−14] Put forth to explain the

occurrence of an exceptionally long-lived light-induced excited state spin trapping (LIESST),[15−17] this effect has now been integrated into synthetic protocols targeting molecular electronics,[18−22] host−guest interactions,[23−25] and self-assembly.[26] Optimizing the design strategies would generally require a detailed characterization of the anisotropy. For $[FeN_6]$ and $[CoN_6]$ SCO complexes, the deformation of the polyhedron subtended by the FCS has been gauged by crystallography through global structural parameters, such as d_G, the distance between the metal atom and the center of gravity of the six N atoms, $\Sigma = \sum_{i=1}^{12} |90 - \phi_i|$, the sum of the angular deviations from 90° for the 12 cis angles ϕ_i, or $\nu = 100 \cdot (1 - \pi(V_P/V_S))$, the deviation of the octahedron from its ideal shape, where V_P and V_S are respectively the volumes of the octahedron and circumscribed sphere. However, the evaluation of these descriptors tends to be strongly affected by incomplete spin-state conversion.[27] Moreover, this particular approach is not applicable to SCO materials lacking long-range order, such as biomolecules,[28−30] polymers,[31] metallomesogens,[32] or small nanoparticles.[33] Being an element-specific probe of the local bonding environment in any physical phase, X-ray absorption

(XA) spectroscopy has often been employed to follow R_{Av} across SCO transitions.[2] After reaching the picosecond and, recently, the femtosecond temporal resolution, it has successfully complemented optical and Raman ultrafast spectroscopies[34] in tracking the HS state of several $[Fe^{II}N_6]$ compounds, which undergo isotropic M–L bond lengthening upon excitation, e.g., $[Fe(bpy)_3]^{2+}$ (bpy: 2,2′-bipyridine),[35−40] $[Fe(phen)_3]^{2+}$ (phen: 1,10-phenanthroline),[41] and $[Fe(tren-(py)_3)]^{2+}$ (tren(py)$_3$: tris(2-pyridin-2-ylmethanimino)ethyl) amine).[42] By applying this technique to photoexcited $[Fe(terpy)_2]^{2+}$ (terpy: 2,2′:6′,2″-terpyridine), the present work demonstrates how the analysis of the XA spectral line shape can differentiate between isotropic and anisotropic bond length elongations, thereby monitoring directly the ultrafast dynamical distortion around the metal center.

■ MATERIALS AND METHODS

Samples. $[Fe(terpy)_2](PF_6)_2$[43] and $[Fe(bpy)_3](PF_6)_2$[44] were synthesized according to the published protocols. All reagents were used as received from commercial sources without further purification.

Femtosecond Transient Absorption Spectroscopy. The femtosecond laser setup used for transient absorption spectroscopy has been previously described.[45] The excitation beam was depolarized and set to 527 nm. For these optical measurements, the time-dependent signals were fitted to a multiexponential function, $f(t) = \sum_i A_i \exp(-t/\tau_i)$, convoluted with a Gaussian instrument response function of 120 fs fwhm.

Picosecond X-ray Absorption Spectroscopy. The time-resolved XA spectroscopy measurements were carried out at beamline 11-ID-D of the APS (Argonne National Laboratory).[46] The optical pump pulse consisted of the second harmonic output of a Nd:YLF regenerative amplified laser at 1.6 kHz repetition rate, giving 527 nm laser pulses with 5 ps fwhm. The X-ray probe pulses with 80 ps fwhm and 6.5 MHz repetition rate were derived from the electron bunches stored in the APS ring. $[Fe(terpy)_2](PF_6)_2$ was dissolved in acetonitrile (MeCN) to reach 1.7 mM. This concentration ensured that the signal was not distorted by self-absorption effects (see X-ray detection below). The liquid sample was flowed through a stainless steel tube and formed a free jet of 550 μm diameter inside an airtight aluminum chamber. The sample was degassed by bubbling nitrogen. The X-ray spot size was 50 μm (V) × 450 μm (H), and the laser spot was 850 μm in diameter. The X-ray and optical beams were overlapped spatially on the replenishing sample. The time delay Δt between the laser and X-ray pulses was fixed by a programmable delay line (PDL-100A-20NS, Colby Instruments) that adjusted the phase shift of the mode-lock driver for the seed laser relative to that of the RF signal of the storage ring with a precision of 500 fs. The incident X-ray energy was stepped through the Fe K edge (7112 eV) up to 700 eV above the 1s threshold. A Fe metal foil placed between two conventional ionization chambers downstream was used for X-ray energy calibration and flux monitoring purposes in transmission mode. Two avalanche photodiodes (APDs) were positioned at 90° angle on both sides of the incident X-ray beam to collect the emitted X-ray fluorescence signals. A [Soller slits/(Z-1) Mn filter] combination, which was custom-designed for the specific sample chamber configuration and the distance between the sample and the detector, was inserted between the sample jet and the APD detectors. This greatly reduced the background due to elastic X-ray scattering. An additional APD was

employed to monitor the intensity of the incident X-ray beam. The outputs of the APDs were sent to two fast analyzer cards (Agilent) that were triggered by a signal at 1.6 kHz from the scattered laser light onto a photodiode. The card digitized the X-ray fluorescence signals as a function of time at 1 ns/point after each trigger. The fluorescence signals from the synchronized X-ray pulse at a 200 ps delay after the laser pump pulse excitation were accumulated to build the XA trace $\mu(laser_{ON})$. The fluorescence signals from the same X-ray pulse averaged over 50 round trips in the storage ring prior to the laser pulse were recorded to build the corresponding XA trace $\mu(laser_{OFF})$. With this collection scheme, the $\mu(laser_{ON})$ and $\mu(laser_{OFF})$ data were taken under the exact same experimental conditions for sample, laser, and beamline, with the shot-to-shot normalization of the X-ray pulse intensities performed by the acquisition software. This allowed canceling out any error associated with drifts. Analyzing the difference signal $\Delta\mu = [\mu(laser_{ON}) - \mu(laser_{OFF})]$ originating from the fraction α of molecules in the excited state delivers the XA spectrum of the photoinduced HS state of $[Fe(terpy)_2]^{2+}$. The integrity of the sample over time was checked by comparing from scan to scan the line shapes of the XA trace $\mu(laser_{OFF})$ in the XANES region. No change due to radiation damage could be detected throughout the duration of the experiment

Fitting Procedure for the Transient X-ray Absorption Spectra. The general procedure for extracting photoinduced structural changes by fitting directly the transient difference XA spectrum $\Delta\mu = [\mu(laser_{ON}) - \mu(laser_{OFF})]$ has been previously presented.[47−49] For the $[Fe^{II}N_6]$ complexes under study, the excited state fraction of photoinduced HS state (α) was first determined independently by minimizing the difference D

$$D = \sum_{i=1}^{N} \frac{1}{\sigma i} [\Delta\mu(i) - \alpha \times \text{ref}(i)]$$

where N is the number of data points, σ_i are the variances estimated from the experimental error bars, and ref is the reference trace constructed in the Supporting Information. The Fe–N$_{Axial}$ and Fe–N$_{Distal}$ bond distances noted R_{Axial} and R_{Distal} and the bite angle N$_{Distal}$ –Fe–N$_{Axial}$ noted β were taken as the sole varying structural parameters. Different model-dependent constraints were imposed between their variations as described in the main text. A molecular editor was used to generate the corresponding x, y, z coordinates for all the geometries. FEFF 9.0[50−52] calculations of the XA profile for the DFT-optimized LS ground state were performed to adjust the nonstructural parameters to match the experimental spectrum. The simulations of the profiles for each of the molecules with a modified Fe coordination sphere were then run, giving the sim traces. The experimental and simulated profiles were interpolated on a grid equally spaced in k, as for steady-state XA data collection, although no FFT was later on applied. This ensured that the spectra of the references and the reconstructed excited state could be processed using the conventional XA softwares Athena and Artemis.[52] The pseudo chi-square function

$$\text{chi}_2 = \sum_{k=2}^{9} \frac{k^2}{\sigma_k} [\Delta\mu(k) - \alpha \times \text{sim}(k)]$$

was calculated as a function of ΔR_{Av}. The statistically correct estimation of all the variances from the experimental error bars is not straightforward and had to be omitted at this stage of the

analysis. This awaits for benchmarking very systematically and carefully the combined influence of not only the detection systems on the time-resolved signal but also the effect of sampling and resampling schemes in E and k space necessarily introduced for fitting. Such work is currently in progress. Nevertheless, renormalizing the chi$_2$ values to the minimum value reached for the best ΔR_{Av} allows using this indicator as a conventional chi-square χ^2 estimate.[53] The values for which chi$_2$ = 2 are the limits of the $1 - \sigma$ confidence interval.

DFT Optimization. The DFT calculations were performed with the ADF program package,[54,55] using the RPBE functional[56] and the Slater-type TZP basis set of triple-ζ polarized quality[57,58] from the ADF basis set database. Solvent effects were taken into account using the conductor-like screening model (COSMO)[59−61] as implemented in ADF.[62] The parameters of the COSMO solvation model were left to their default values.

■ RESULTS AND DISCUSSIONS

Establishing the origin of SCO in the coupling between electronic and geometric structures has been one of the striking successes of ligand field theory in generalizing molecular orbital theory to describe d^4-d^7 transition metal complexes. As a first approximation, an octahedral (O_h) ligand field (LF) lifts the degeneracy of the d levels, which are split into t_{2g} and e_g levels. The balance between the ligand field splitting energy (LFSE) and the mean spin pairing energy determines the orbital occupation numbers, hence the term multiplicity of the ground state. In $[Fe^{II}N_6]$ systems, a strong LF stabilizes the $(t_{2g})^6\,{}^1A_1$ LS state, while a weak LF favors the $(t_{2g})^4(e_g)^2\,{}^5T_2$ HS state. At intermediate LS strength, the energetic gap separating the two manifolds becomes comparable to kT so that an entropy-driven transition yields an equilibrated Boltzmann distribution of the two spin states.

Single crystal X-ray diffraction shows that the $[Fe(terpy)_2]^{2+}$ cation possesses D_{2d} symmetry in the $(t_{2g})^6\,{}^1A_1$ low-spin (LS) ground state.[63] The axial distortion from ideal O_h symmetry arises from steric and electronic constraints imposed by the meridional coordination of the planar tridentate ligand. As illustrated in Figure 1, the preferential covalent back-donation
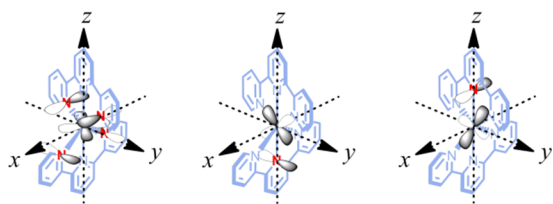

Figure 1. Schematic illustrating the preferential π back-bonding of the central Fe atom with the N_{axial} atoms.

from the metal d_{yz} and d_{xz} to the π^* terpy orbitals renders Fe−N_{Axial} (1.89 Å) significantly shorter than Fe−N_{Distal} (1.98 Å), with *cis* bond angles of 75−80° and *trans* bond angles of 165°. The uneven repartition of π electronic density is detected via a large Mössbauer quadrupole splitting.[16]

Figure 2a displays the normalized Fe K edge XA spectrum μ of $[Fe(terpy)_2]^{2+}$ in acetonitrile (MeCN) (gray trace), which remains in the LS state upon solvation. Despite the tetragonal distortion of the FCS, the weak pre-edge signal appears as a single peak (P), in close similarity to the one observed for the tris-chelate ferrous complexes, validating a quasi-O_h description
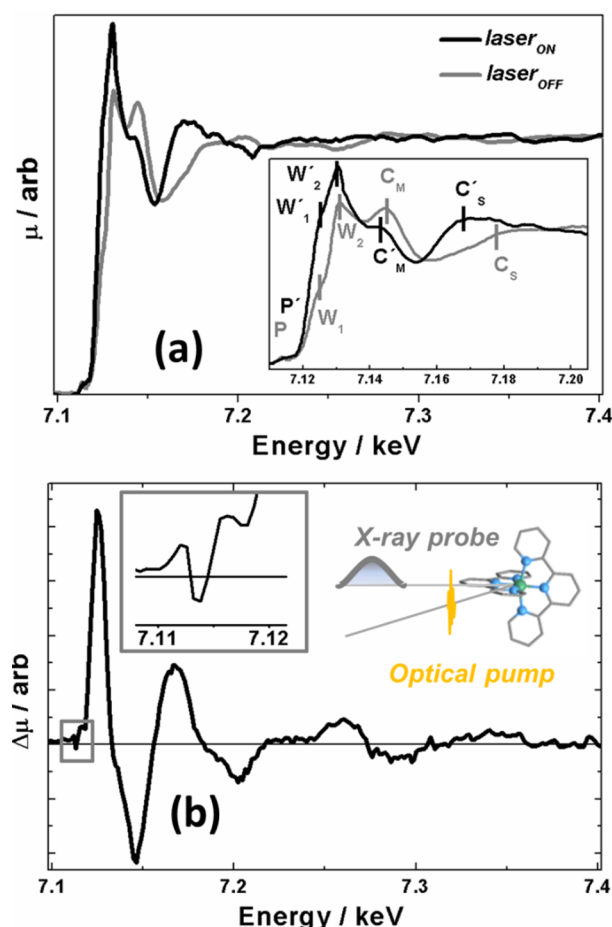

Figure 2. (a) Normalized X-ray absorption (XA) spectrum μ without (gray) and with (black) laser illumination for $[Fe(terpy)_2]^{2+}$ in MeCN, at a pump−probe time delay of 200 ps. The inset zooms on the near-edge region. (b) Difference XA (DXA) spectrum $\Delta\mu$. The inset zooms on the pre-edge region.

of the LS ground state. The intensity of P is attributed to the quadrupole-allowed $1s \rightarrow 3d$ transition,[64] which usually gains additional oscillator strength with 3d−4p mixing (i.e., loss of centrosymmetry). Between ∼5 and ∼100 eV above the absorption edge, the distinctive spectral features of LS $[Fe^{II}N_6]$ complexes are observed.[35−42] They can be assigned using a simple expression of the molecular orbitals (MO) as linear combinations of atomic orbitals (LCAO),[65] and more precisely, through ab initio multiple scattering calculations[42] or time-dependent DFT (TD-DFT) modeling.[66,67] In the near-edge (XANES) region, features W_1 (∼7125 eV) and W_2 (∼7130 eV) are ascribed to the promotion of the core electron to the lowest unoccupied states derived from Fe(4s,4p) and N(2p) hybridization. Features C_S (∼7178 eV) and C_M (∼7145 eV) can be traced back to single and multiple scattering of the outgoing photoelectron within the FCS. Upon pulsed laser excitation at λ = 527 nm, the ^{1}MLCT Franck−Condon state is formed instantaneously and the complex relaxes to the $(t_{2g})^4(e_g)^2\,{}^5T_2$ high-spin (HS) state on the subpicosecond time scale.[68] Displayed in Figure 2a (black trace), the transient signal recorded for an optical pump−X-ray probe time delay of 200 ps reflects the coupled electronic and nuclear rearrangements that take place in the HS state. This lowest-energy excited state does not have a charge-transfer character.[69] The amplitude of the difference XA (DXA) spectrum $\Delta\mu$ =

$[\mu(laser_{ON}) - \mu(laser_{OFF})]$ is shown in Figure 2b. Charge depletion from the t_{2g} slightly bonding orbitals and population of the e_g antibonding orbitals concurrently trigger a marked expansion of the FCS revealed by the evolution of features C_S and C_M into C_S' ($\sim$7168 eV) and C_M' ($\sim$7142 eV). The associated reduction in spatial overlap with N(2p) induces a stabilization of Fe(4s,4p), which is evidenced by the slight energy downshift of the rising edge W_1' ($\sim$7124 eV). It also causes an increase in unoccupied p-density of states manifested by a more intense white line W_2' ($\sim$7130 eV).

Figure 3a displays the kinetics acquired at W_1', C_M, and C_S'. A global fit including the convolution with the machine
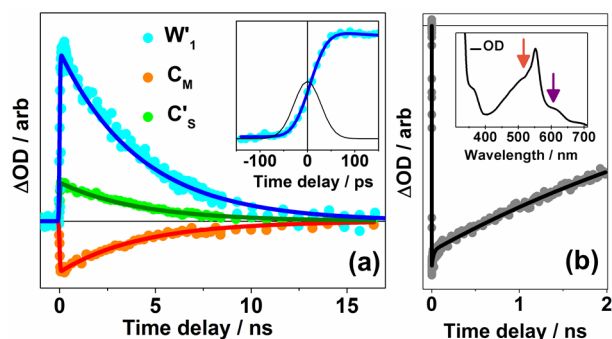

Figure 3. (a) X-ray kinetics acquired at photon energies W_1' (blue), C_M (orange), and C_S' (green). The inset zooms on the rise at early times, with the Gaussian X-ray pulse used for the convolution of the single-exponential fit. (b) Ground state bleach recovery monitored with transient optical spectroscopy. The UV–vis spectrum is given in the inset, where the wavelengths of the pump (527 nm) and the probe (600 nm) are indicated by arrows.

response function (80 ps fwhm) retrieves a single-exponential time constant of 4.21 ± 0.04 ns. This value is in agreement with the 4.50 ± 0.16 ns obtained by monitoring the ground state bleach recovery HS → LS using transient optical absorption spectroscopy (Figure 3b).

Being roughly proportional to $1/R_{av}^6$ for neutral ligands,[70,71] the LFSE of $[Fe(bpy)_3]^{2+}$, $[Fe(phen)_3]^{2+}$, and $[Fe(terpy)_2]^{2+}$ are comparable (12 650, 12 700, and 12 350 cm^{-1}, respectively).[72,73] However, the zero-point energy gap between the LS and HS states is also affected by the nature of the ligands and the surrounding.[70,71] Since this parameter modulates the second-order spin orbit coupling involved in the net $\Delta S = 2$ conversion,[9] the nonradiative ground state recovery dynamics are influenced by conformational reorganization, and the HS lifetimes across this class of compounds significantly differ by up to an order of magnitude depending on the solvent.[74,75] This fact is illustrated by Figure 4, which displays the normalized X-ray kinetics taken at W_1' for equimolar solutions (1.7 mMol) of $[Fe(bpy)_3]^{2+}$ and $[Fe(terpy)_2]^{2+}$ in MeCN (see the Supporting Information). Under the same experimental conditions, the lifetime of $[Fe(bpy)_3]^{2+}$ and $[Fe(terpy)_2]^{2+}$ are fitted to 1.37 ± 0.04 ns and 4.25 ± 0.05 ns, respectively.

Accommodating the rigidity of the terpy ligand restricts the evolution of the structural parameters Fe–N$_{Axial}$ (R_{Axial}), Fe–N$_{Distal}$ (R_{Distal}), and N$_{Distal}$–Fe–N$_{Axial}$ (bite angle β); hence, their variations ΔR_{Axial}, ΔR_{Distal}, and $\Delta\beta$ are not independent from each other as shown in Figure 5a. Hypothetically, for an isotropic expansion of the FCS, R_{Axial} and R_{Distal} increase by the same ΔR, while β remains constant (path I in Figure 5b and 5c). Two approaches can be devised to extract the actual

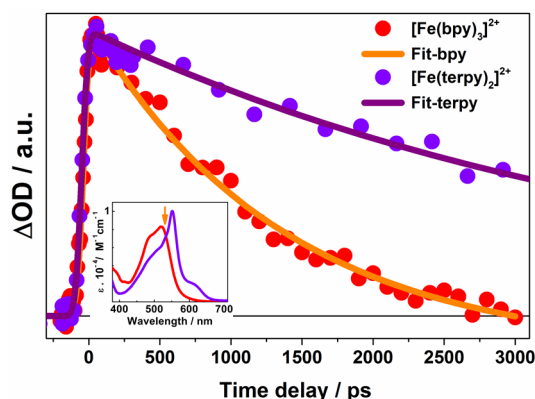**Figure 4.** X-ray kinetics acquired at 7124 eV for $[Fe(bpy)_3]^{2+}$ (data, red dots; single exponential fit, orange line) and $[Fe(terpy)_2]^{2+}$ (data, violet dots; single exponential fit, purple line). The extinction coefficients of $[Fe(bpy)_3]^{2+}$ (red) and $[Fe(terpy)_2]^{2+}$ (purple) in MeCN are given in the inset. The arrow indicates the wavelength of the excitation used in the XA pump−probe measurements.
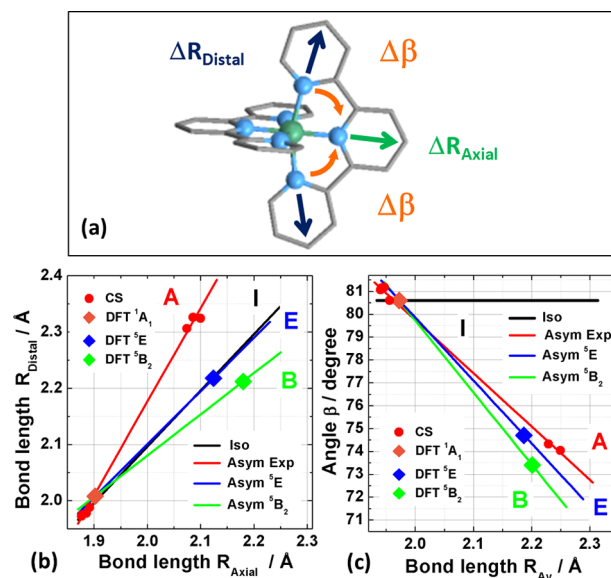

Figure 5. (a) Schematic illustrating the variations in structural parameters ΔR_{Axial}, ΔR_{Distal}, and $\Delta\beta$ considered in the analysis. (b) Empirical (respectively theoretical) linear correlation between R_{Axial} and R_{Distal} and (c) between R_{Av} and the bite angle β. The red dots (respectively blue and green diamonds) indicate the parameters extracted from published crystal structures (CS) (respectively from DFT optimization). The constraints imposed between ΔR_{Axial}, ΔR_{Distal}, and $\Delta\beta$ during the modeling of $\Delta\mu$ are indicated as paths I (black), A (red), E (blue), and B (green).

correlations induced by the terpy coordination in the condensed phase. The first one is based on empirical findings from SCO synthetic chemistry. Extensive work has demonstrated how specific ring substitutions within the terpy unit are tuning the LFSE, so that the ground state of these tridentate complexes becomes HS.[76−81] From the reported crystallographic structures of these compound families, a linear correlation is found between R_{Axial} and R_{Distal}, as well as between R_{Av} and β (path A in Figure 5b and 5c). It should be noted that counterions and residual solvent molecules, along with crystal packing forces, might influence these structures,

although such effects have not been reported so far as dominating for the terpy embrace.[82]

The second approach is based on DFT calculations. Most post-LDA functionals give excellent results for determining the geometry of transition metal complexes.[83−85] The present DFT optimization of $[\text{Fe(tepy)}_2]^{2+}$ in MeCN was performed with the RPBE functional assuming a D_{2d} symmetry.[17] This choice was made in light of previous work on $[\text{Fe(bpy)}_3]^{2+}$ testing various functionals, where RPBE proved to be one of the few that can give satisfying results for the energy difference between the LS and HS states.[85] The geometries of the complex in the LS $^1A_1$ state and in the $^5B_2$ and ^5E tetragonal components of the HS state were optimized with the molecular symmetry constrained to D_{2d}. The vibrational analysis performed on the optimized LS geometry establishes that this geometry corresponds to a true minimum (the calculated frequencies are all real). The calculated ^5E geometry is Jahn−Teller unstable. The vibrational analysis performed on the $^5B_2$ geometry shows that it corresponds to a transition state. The vibrational instability of the $^5B_2$ state probably results from its pseudo-Jahn−Teller coupling with the close-lying degenerate ^5E state. The study of the vibronic instability in the HS manifold is beyond the scope of this study. Furthermore, this phenomenon is not expected to alter the conclusions drawn here regarding the changes experienced by the FCS of the complex. Indeed, the results of geometry optimizations performed in D_2 and in C_{2v} for the complex in the HS state indicate that the vibronic instability mainly leads to minor differences with the reported D_{2d} calculated geometries. The atom labeling used is shown in Figure 6. The results are compiled in Table 1 given below.
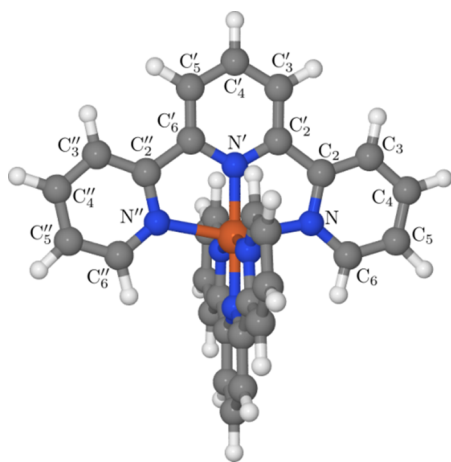

Figure 6. $[\text{Fe(terpy)}_2]^{2+}$ complex with the atom labeling used in the DFT optimization.

Compared to the ^5E state, the $^5B_2$ state presents a longer R_{Axial}, a similar R_{Distal}, and a slightly lower total energy. The calculated geometric parameters are in excellent agreement with other investigations.[83,84] The linear correlations imposed between R_{Axial} and R_{Distal}, as well as between R_{Av} and β during a transition from $^1A_1$ to ^5E (path E) and from $^1A_1$ to $^5B_2$ (path B), are also shown in Figure 5b and 5c. Experimentally, the distortion of the FCS in the photoinduced HS state can be characterized by fitting the k^2-weighted $\Delta\mu(k)$ displayed in Figure 7a (gray trace). Calibrating against $[\text{Fe(bpy)}_3]^{2+}$ measured under the same experimental conditions (dark red

Table 1. Electronic Energy Differences between the LS $^1A_1$ and the HS $^5B_2$ and ^5E States of D_{2d} $[\text{Fe(terpy)}_2]^{2+}$ and Selected Structural Parameters

	$^5B_2$		^5E
ΔE_{el} (cm^{-1})	8340		9245
	$^1A_1$	$^5B_2$	^5E
Fe−N, Fe−N″ (Å)	2.008	2.212	2.218
Fe−N′ (Å)	1.902	2.180	2.124
N−C$_2$, N″−C$_2$″ (Å)	1.378	1.365	1.366
N−C$_6$, N″−C$_6$″ (Å)	1.355	1.351	1.351
C$_2$−C$_3$, C$_2$″−C$_3$″ (Å)	1.403	1.404	1.406
C$_3$−C$_4$, C$_3$″−C$_4$″ (Å)	1.399	1.401	1.400
C$_4$−C$_5$, C$_4$″−C$_5$″ (Å)	1.402	1.401	1.402
C$_5$−C$_6$, C$_5$″−C$_6$″ (Å)	1.398	1.399	1.399
C$_2$−C$_2$′, C$_6$′−C$_2$″ (Å)	1.470	1.489	1.487
N′−C$_2$′, N′−C$_6$′ (Å)	1.366	1.356	1.360
C$_2$′-C$_3$′, C$_5$′-C$_6$′ (Å)	1.403	1.405	1.404
C$_3$′-C$_4$′, C$_4$′−C$_5$′ (Å)	1.402	1.400	1.400
(C$_6$′-C$_2$″, C$_2$-C$_2$′) (°)	102.9	107.9	108.6
(N′−Fe−N) = (N″−Fe−N′) (°)	80.6	73.4	74.7
(N″−Fe−N) (°)	161.2	146.8	149.4
(N′−C$_2$′−C$_2$−N) = (N″−C$_2$″-C$_6$′−N′) (°)	0.0	0.0	0.0

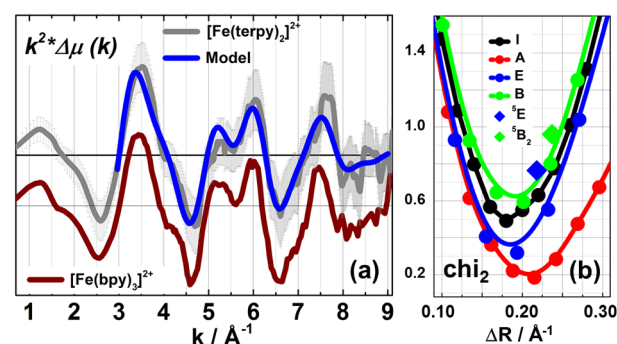**Figure 7.** Analysis of the EXAFS fingerprints. (a) Experimental k^2*DXA spectrum for $[\text{Fe(terpy)}_2]^{2+}$ (gray) and $[\text{Fe(bpy)}_3]^{2+}$ (dark red). The blue line shows the k^2*DXA spectrum simulated from the ^5E HS state obtained through DFT optimization. (b) The chi$_2$ factors calculated along paths A, I, E, and B (red, black, blue, and green line-connected dots) and for the DFT-optimized structures (diamonds).

trace) enables determining $85 \pm 5\%$ as the excited state fraction (see details in the Supporting Information), a parameter necessary for the analysis of the XA line shape. Figure 7a also evidences the subtle EXAFS signatures of the anisotropic change in bond length that manifests as differences in oscillation amplitudes and a slow relative dephasing. The fitting procedure consists in finding the molecular structure that minimizes in k space the chi$_2$ factor of the difference between its $k^2*\Delta\mu(k)$ and the experimental one. The search across the parameter space spanned by R_{Axial}, R_{Distal}, and β was confined to geometries where the incremented variations ΔR_{Axial}, ΔR_{Distal}, and $\Delta\beta$ followed either path I ($\Delta R_{\text{Distal}} = \Delta R_{\text{Axial}}$; $\Delta\beta = 0$), path A ($\Delta R_{\text{Distal}} = 1.151 \cdot \Delta R_{\text{Axial}}$; $\Delta\beta = -23.83 \cdot \Delta R_{\text{Av}}$), path E ($\Delta R_{\text{Distal}} = 0.946 \cdot \Delta R_{\text{Axial}}$; $\Delta\beta = -27.57 \cdot \Delta R_{\text{Av}}$), or path B ($\Delta R_{\text{Distal}} = 0.734 \cdot \Delta R_{\text{Axial}}$; $\Delta\beta = -31.48 \cdot \Delta R_{\text{Av}}$), while the ligand rings were rigidly displaced. The respective $k^2*\Delta\mu(k)$ were simulated with FEFF9.0 multiple scattering calculations.[86] The resulting chi$_2$ factors are displayed in Figure 7b, along with the ones extracted from the ^5E and $^5B_2$ DFT-optimized structures. The importance of incorporating the ligand deformation in the

analysis is apparent, since the chi$_2$ of both theoretical structures fall outside the curves obtained for rigid displacements of the terpy rings on paths E and B. In addition, Figure 7b suggests possible limitations to the use of chemically stabilized spin-state for the EXAFS analysis of anisotropic distortions. Overall, the results indicate that the photoinduced HS state most likely adopts a ^{5}E geometry, although covering a longer k range with increased S/N ratio is the clear target of upcoming work.

The difference XANES (DXANES) profile generated from the atomic coordinates of this ^{5}E state is shown in Figure 8a (blue trace). The unoccupied p-density of states (p-DOS) at the Fe and N atoms displayed in Figure 8b and 8c corroborate the simple LCAO-MO interpretation.
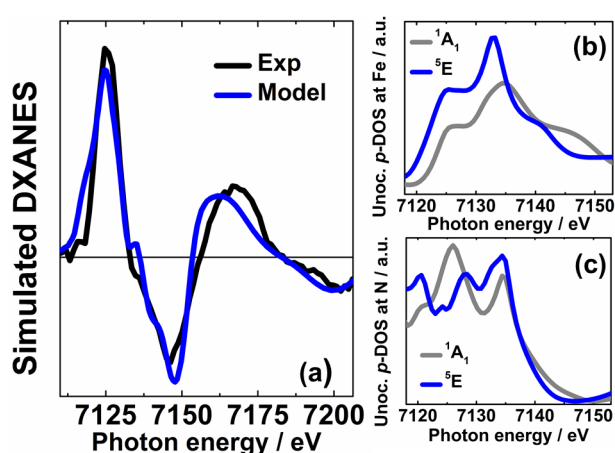

Figure 8. Analysis of the XANES fingerprints. (a) Simulated difference XANES (DXANES) spectrum for the DFT-optimized ^{5}E HS state (blue) and experimental (black) spectra. (b) Associated unoccupied p-DOS at the Fe atom for the ^{1}A$_1$ LS (gray) and the ^{5}E HS state (blue). (c) Similarly, at the N atoms.

A complementary view into the photoinduced atomic rearrangements and the charge redistribution within the d levels is found in the pre-edge region, which is sensitive to the electronic structure.[64] Figure 9a shows this transient signal for
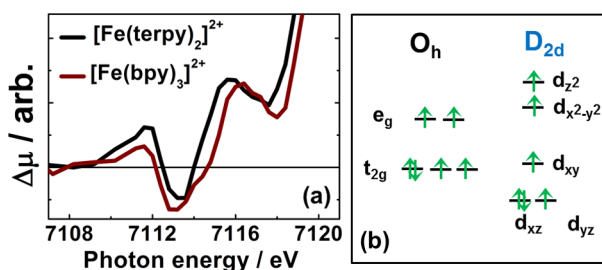

Figure 9. Qualitative analysis of the pre-edge fingerprints. (a) Transient signal in the pre-edge region for [Fe(terpy)$_2$]$^{2+}$ (black) and [Fe(bpy)$_3$]$^{2+}$ (dark red). (b) Schematic illustrating the splitting of the t$_{2g}$ and e$_g$ orbitals upon symmetry lowering from O_h to D_{2d}.

[Fe(bpy)$_3$]$^{2+}$ and [Fe(terpy)$_2$]$^{2+}$. In HS ferrous complexes of O_h and quasi-O_h symmetries, the features underlying the 1s → 3d peak are attributed to the three strong-field multiplets of the $(1s)^{-1}(3d)^7$ configuration: $(1s)^{-1}(t_{2g})^5(eg)^2 \cong (t_{2g})(eg)^2$ $(^4T_{1g})$ and $(1s)^{-1}(t_{2g})^4(eg)^3 \cong (t_{2g})^2(eg)^3(^4T_{1g}, {}^4T_{2g})$. The overall splitting, ~2 eV, is directly related to the LFSE of the $(1s)^{-1}(3d)^7$ state, generally unknown but estimated to be about 80% of the ground state value.[64] Studies on photoinduced HS

species have so far reported transient changes in agreement with such a set of energy levels (e.g., for [Fe(bpy)$_3$]$^{2+}$,[39] [Fe(phen)$_3$]$^{2+}$,[41] and [Fe(tren(py)$_3$)]$^{2+}$).[42] State-of-the-art TD-DFT modeling of the 1s → 3d transition in [Fe(bpy)$_3$]$^{2+}$ has ascribed the positive feature at 7112 eV to the accessible 1s → t$_{2g}$ transitions.[66] The origin of the larger oscillator strength observed for [Fe(terpy)$_2$]$^{2+}$ may be associated with the symmetry lowering to D_{2d} since the uniaxial deformation stabilizes the (d$_{xz}$, d$_{yz}$) set (Figure 9b). The changes in covalent σ donation and π back-donation, which have been reported in the XA experiments at the Fe L edge and N K edge in the soft X-ray range,[87−89] also influence the relative positions and intensities of the underlying transitions. However, ascertaining their exact assignment will require further theoretical progress, such as incorporating quadrupole transitions in the treatment of the 1s → 3d transition[66] and developing the ab initio description of 2p XA spectra for first-row transition metal complexes.[68]

■ **CONCLUSION**

In summary, the transient HS state of solvated [Fe(terpy)$_2$]$^{2+}$ has been observed using picosecond XA spectroscopy. This work demonstrates on a tractable example that the technique can map out the anisotropic structural dynamics of photo-induced SCO transitions on their intrinsic time scale, thereby complementing other ultrafast techniques.[40,90−93] The analysis based on line shape modeling with multiple scattering calculations captures the distortion of the FCS and indicates that the complex most likely adopts in the HS state the ^{5}E geometry predicted by DFT calculations. Aside from its practical importance as versatile building block of birefringent coordination polymers[94] and metallo-supramolecular polyelectrolytes,[95−97] the role of [Fe(terpy)$_2$]$^{2+}$ as experimental and theoretical benchmark has considerably increased in the field of solar energy conversion. Recently, novel synthetic strategies employing σ donor ligands such as dcpp (2,6-bis(2-carboxypyridyl)pyridine),[98] (N^C^N)$^-$,[99] or (C^N^C)[100] have emerged. These compounds exhibit extremely promising photophysical behavior, and the rationalization of their electronic and geometric structures is currently achieved by comparison with the simpler tridentate complex [Fe(terpy)$_2$]$^{2+}$. It can then be expected that ultrafast XA spectroscopy will play an immediate role in the characterization of such systems and, more generally, in the optimization of a wide range of photoactive molecular complexes based on abundant and cost-effective low-Z elements. The outlined methodology will also be particularly suited to the study of spin changes triggered by short-range interactions, such as ligand-driven SCO.[101] Uncovering the complete reaction coordinate of the spin-state interconversion in [Fe^{II}N$_6$] complexes will necessitate refining the description of the ultrafast structural dynamics on multiple length scales, including the concurrent vibrational excitation of the high-frequency modes and of an ill-delimited fraction of the low-frequency modes that involve the ligands and the surrounding solvent cage. This can be partly achieved by combining XA spectroscopy with X-ray emission (XE) and X-ray diffuse scattering (XDS).[40] The independent determination of the HS fraction in the probed volume through XE reduces the correlation between the structural parameters of the solute extracted from XA and XDS measurements (e.g., the high-frequency Fe−N stretch).[40] The reorganization of the first solvation shell can be monitored by XDS[40] and now modeled with ab initio Molecular Dynamics calculations.[102] In addition,

XDS can track the excess energy lost to the surrounding as heat.[40,103,104] Finally, such investigations on solvated complexes in the homogeneous phase will be assisting the exploration of SCO phenomena in the solid phase, known to be complicated by the noncovalent interactions that promote the emergence of cooperativity and memory effects.

■ ASSOCIATED CONTENT

Ⓢ Supporting Information

Determination of the excited state fraction in the picosecond XA experiment. This material is available free of charge via the Internet at http://pubs.acs.org.

■ AUTHOR INFORMATION

Corresponding Author

*E-mail: Sophie.Canton@maxlab.lu.se (S.E.C); xyzhang@aps.anl.gov (X.Z.); villy.sundstrom@chemphys.lu.se (V.S.).

Notes

The authors declare no competing financial interest.

■ ACKNOWLEDGMENTS

■ REFERENCES

(1) van Koningsbruggen, P. J.; Maeda, Y.; Oshio, H. Iron(III) Spin Crossover Compounds. *Top. Curr. Chem.* **2004**, *233*, 259−324.

(2) Gütlich, P.; Goodwin, H. A. Spin Crossover—An Overall Perspective. *Top. Curr. Chem.* **2004**, *233*, 1−47.

(3) Halcrow, M. A. Structure:Function Relationships in Molecular Spin-Crossover Complexes. *Chem. Soc. Rev.* **2011**, *40*, 4119−4142.

(4) Létard, J.-F.; Guinneau, P.; Goux-Capes, L. Towards Spin Crossover Applications. *Top. Curr. Chem.* **2004**, *235*, 221−249.

(5) Beattie, J. K.; Binstead, R. A.; West, R. J. Intersystem Crossing Observed by Ultrasonic Relaxation of the Singlet−Quintet Spin Equilibrium of Iron(II) Complexes in Solution. *J. Am. Chem. Soc.* **1978**, *100*, 3044−3050.

(6) Hoselton, M. A.; Drago, R. S.; Wilson Sutin, N. Direct Measurement of Spin-State Lifetimes in Solution for Iron(II) Spin Equilibrium Complexes Derived from Hexadentate Ligands. *J. Am. Chem. Soc.* **1976**, *98*, 6967−6969.

(7) Warner, B.; Oberg, J. C.; Gill, T. G.; El Hallack, F.; Hirjigehedin, C. F.; Seeri, M.; Heutz, S.; Arrio, M. A.; Sainctavit, P.; Mannini, M. M.; et al. Temperature-and Light-Induced Spin Crossover Observed by X-Ray Spectroscopy on Isolated Fe(II) Complexes on Gold. *J. Phys. Chem. Lett.* **2013**, *4*, 1546−1552.

(8) Brady, C.; McGarvey, J. J.; McCusker, J. K.; Toftlund, H.; Hendrikseh, D. N. Time-Resolved Relaxation Studies of Spin Crossover Systems in Solution. *Top. Curr. Chem.* **2004**, *253*, 1−21.

(9) Buhks, E.; Navon, G.; Bixon, M.; Jortner, J. Spin Conversion Processes in Solutions. *J. Am. Chem. Soc.* **1980**, *102*, 2918−2923.

(10) Marchivie, M.; Guionneau, P.; Létard, J.-P.; Chasseau, D. Towards Direct Correlations Between Spin-Crossover and Structural

(11) Alvarez, S. Relationships between Temperature, Magnetic Moment, and Continuous Symmetry Measures in Spin Crossover Complexes. *J. Am. Chem. Soc.* **2003**, *125*, 6795−6802.

(12) Bernien, M.; Wiedemann, D.; Hermanns, C. F.; Krueger, A.; Rolf, D.; Kroener, W.; Mueller, P.; Grohmann, A.; Kuch, W. Spin Crossover in a Vacuum-Deposited Submonolayer of a Molecular Iron(II) Complex. *J. Phys. Chem. Lett.* **2012**, *3*, 3431−3434.

(13) Marchivie, M.; Guionneau, P.; Létard, J.-F.; Chasseau, D. Photoinduced Spin-Transitions: The Role of the Iron(II) Environment Distortion. *Acta Crystallogr., Sect. B: Struct. Sci.* **2005**, *61*, 25−28.

(14) Hou, J.; Wang, Q.; Sun, Q.; Kawazoe, Y.; Jena, P. J. Strain-Induced Spin Crossover in Phtalocyanine-Based Organometallic Sheets. *J. Phys. Chem. Lett.* **2012**, *3*, 3109−3114.

(15) Renz, F.; Oshio, H.; Ksenofontov, V.; Waldeck, M.; Spiering, H.; Gütlich, P. Strong Field Iron(II) Complex Converted by Light into a Long-Lived High-Spin State. *Angew. Chem., Int. Ed.* **2000**, *39*, 3699−3700.

(16) Oshio, H.; Spiering, H.; Ksenofontov, V.; Renz, F.; Gütlich, P. Electronic Relaxation Phenomena Following Co-57(EC)Fe-57 Nuclear Decay in [Mn-II(terpy)(2)](ClO$_4$)(2) (1)/2H$_2$O and in the Spin Crossover Complexes [Co-II(terpy)(2)]X−2 nH(2)O (X = Cl and ClO$_4$): A Mossbauer Emission Spectroscopic Study. *Inorg. Chem.* **2001**, *40*, 1143−1150.

(17) Hauser, A.; Enachescu, C.; Lawson-Daku, M. L.; Vargas, A.; Amstutz, N. Low-Temperature Lifetimes of Metastable High-Spin States in Spin-Crossover and in Low-Spin Iron(II) Compounds: The Rule and Exceptions to the Rule. *Coord. Chem. Rev.* **2006**, *250*, 1642−1652.

(18) Abdul-Kader, K.; Lopes, M.; Bartual-Murgui, C.; Kraieva, O.; Hernandez, E. M.; Salmon, L.; Nicolazzi, W.; Carcenac, F.; Thibault, C.; Molnar, G.; Bousseksou, A. Synergistic Switching of Plasmonic Resonances and Molecular Spin States. *Nanoscale* **2013**, *5*, 5288−5293.

(19) Diefenbach, M.; Kim, K. S. Toward Molecular Magnetic Switches with an Electrical Bias. *Angew. Chem., Int. Ed.* **2007**, *46*, 7640−7643.

(20) Hao, H.; Zheng, X. H.; Song, L. L.; Wang, R. N.; Zeng, Z. Electrostatic Spin Crossover in a Molecular Junction of a Single-Molecule Magnet Fe$^{−2}$. *Phys. Rev. Lett.* **2012**, *108*, 017202.

(21) Baadji, N.; Piacenza, M.; Tugsuz, T.; Della Sala, F.; Maruccio, G.; Sanvito, S. Electrostatic Spin Crossover Effect in Polar Magnetic Molecules. *Nat. Mater.* **2009**, *8*, 813−817.

(22) Schneider, B.; Demeshko, S.; Dechert, S.; Meyer, F. A Double-Switching Multistable Fe$^{−4}$ Grid Complex with Stepwise Spin-Crossover and Redox Transitions. *Angew. Chem., Int. Ed.* **2010**, *49*, 9274−9277.

(23) Southon, P. D.; Liu, L.; Fellows, E. A.; Price, D. J.; Halder, G. J.; Chapman, K. W.; Moubaraki, B.; Murray, K. S.; Letard, J.-F.; Kepert, C. J. Dynamic Interplay between Spin-Crossover and Host−Guest Function in a Nanoporous Metal−Organic Framework Material. *J. Am. Chem. Soc.* **2009**, *131*, 10998−11009.

(24) McHale, R.; Liu, Y. B.; Ghasdian, N.; Hondow, N. S.; Ye, S. J.; Lu, Y.; Brydson, R.; Wang, X. S. Dual Lanthanide Role in the Designed Synthesis of Hollow Metal Coordination (Prussian Blue Analogue) Nanocages with Large Internal Cavities and Mesoporous Cage. *Nanoscale* **2011**, *3*, 3685.

(25) Bao, X.; Sheperd, H. J.; Salmon, L.; Molnar, G.; Tong, M. L.; Bousseksou, A. The Effect of an Active Guest on the Spin Crossover Phenomenon. *Angew. Chem., Int. Ed.* **2013**, *52*, 1198−1202.

(26) Ding, J.; Yang, Y.; Yang, L.; Yan, Y.; Huang, J. B.; Stuart, M. A. C. A Case of Adaptive Self-Assembly. *ACS Nano* **2012**, *6*, 1004−1010.

(27) Legrand, V.; Pillet, S.; Weber, H.-P.; Souhassou, M.; Letard, J.-F.; Guionneau, P.; Lecomte, C. On the Precision and Accuracy of Structural Analysis of Light-Induced Metastable States. *J. Appl. Crystallogr.* **2007**, *40*, 1076−1088.

(28) Caignan, G. A.; Deshmukh, R.; Zeng, Y. H.; Wilks, A.; Bunce, R. A.; Rivera, M. The Hydroxide Complex of Pseudomonas Aeruginosa

Heme Oxygenase as a Model of the Low-Spin Iron(III) Hydroperoxide Intermediate in Heme Catabolism: C-13 NMR Spectroscopic Studies Suggest the Active Participation of the Heme in Macrocycle Hydroxylation. *J. Am. Chem. Soc.* **2003**, *125*, 11842−11852.

(29) Doukov, T.; Li, H. Y.; Sharma, A.; Marte, J. D.; Soltis, S. M.; Silverman, R. B.; Poulos, T. L. Temperature-Dependent Spin Crossover in Neuronal Nitric Oxide Synthase Bound with the Heme-Coordinating Thioether Inhibitors. *J. Am. Chem. Soc.* **2003**, *125*, 11842−11852.

(30) Nakamura, M. Electronic Structures of Highly Deformed Iron(III) Porphyrin Complexes. *Coord. Chem. Rev.* **2006**, *250*, 2271−2294.

(31) Garcia, Y.; Niel, V.; Munoz, M. C.; Real, J. A. Spin Crossover in 1D, 2D, and 3D Polymeric Fe(II) Networks. *Top. Curr. Chem.* **2004**, *233*, 229−257.

(32) Gaspar, A. B.; Seredyuk, M.; Gütlich, R. Spin Crossover in Metallomesogens. *Coord. Chem. Rev.* **2001**, *253*, 2399−2413.

(33) Chakraborty, P.; Boillot, M. L.; Tissot, A.; Hauser, A. Photoinduced Relaxation Dynamics in Iron(II) Spin-Crossover Nanoparticles: The Significance of Crystallinity. *Angew. Chem., Int. Ed.* **2013**, *52*, 7139−7142.

(34) Smeigh, A. L.; Creelman, M.; Mathies, R. A.; McCusker, J. K. Femtosecond Time-Resolved Optical and Raman Spectroscopy of Photoinduced Spin Crossover: Temporal Resolution of Low-to-High Spin Optical Switching. *J. Am. Chem. Soc.* **2008**, *130*, 14105−14107.

(35) Gawelda, W.; Pham, V. T.; Benfatto, M.; Zaushitsyn, Y.; Kaiser, M.; Grolimund, D.; Johnson, S. L.; Abela, R.; Hauser, A.; Bressler, C.; et al. Structural Determination of a Short-Lived Excited Iron(II) Complex by Picosecond X-ray Absorption Spectroscopy. *Phys. Rev. Lett.* **2007**, *98*, 057401.

(36) Bressler, C.; Milne, C.; Pham, V.-T.; El Nahhas, A.; van der Veen, R. M.; Gawelda, W.; Johnson, S.; Beaud, P.; Grolimund, D.; Kaiser, M.; Borca, C. N.; Ingold, G.; Abela, R.; Chergui, M. Femtosecond XANES Study of the Light-Induced Spin Crossover Dynamics in an Iron(II) Complex. *Science* **2009**, *323*, 489−492.

(37) Cannizzo, A.; Milne, C. J.; Consani, C.; Gawelda, W.; Bressler, C.; van Mourik, F.; Chergui, M. Light-Induced Spin Crossover in Fe(II)-Based Complexes: The Full Photocycle Unraveled by Ultrafast Optical and X-ray Spectroscopies. *Coord. Chem. Rev.* **2010**, *254*, 2677−2686.

(38) Lemke, H. T.; Bressler, C.; Chen, L. X.; Fritz, D. M.; Gaffney, K. J.; Galler, A.; Gawelda, W.; Haldrup, K.; Hartsock, R. W.; Ihee, K. J.; et al. Femtosecond X-ray Absorption Spectroscopy at a Hard X-ray Free Electron Laser: Application to Spin Crossover Dynamics. *J. Chem. Phys. B* **2013**, *117*, 735−740.

(39) Lima, F. A.; Milne, C. J.; Amarasinghe, D. C. V.; Rittmann-Franck, M. H.; van der Veen, R. M.; Reinhard, M.; Pham, V. T.; Karlsson, S.; Johnson, S. L.; Grolimund, D.; et al. A High-Repetition Rate Scheme for Synchrotron-Based Picosecond Laser Pump/X-ray Probe Experiments on Chemical and Biological Systems in Solution. *Rev. Sci. Instrum.* **2011**, *82*, 063111.

(40) Haldrup, K.; Vanko, G.; Gawelda, W.; Galler, A.; Doumy, G.; March, A. M.; Kanter, E.; Bordage, A.; Dohn, A.; van Driel, T. B; et al. Guest−Host Interactions Investigated by Time-Resolved X-ray Spectroscopies and Scattering at MHz Rates: Solvation Dynamics and Photoinduced Spin Transition in Aqueous Fe(bipy)(3)(2+). *J. Phys. Chem. A* **2012**, *116*, 9878−9887.

(41) Nozawa, S.; Sato, T.; Chollet, M.; Ichiyanagi, K.; Tomita, A.; Fujii, H.; Adachi, S.; Koshihara, S. Direct Probing of Spin State Dynamics Coupled with Electronic and Structural Modifications by Picosecond Time-Resolved XAFS. *J. Am. Chem. Soc.* **2010**, *132*, 61−63.

(42) Khalil, M.; Marcus, M. A.; Smeigh, A. L.; McCusker, J. K.; Chong, H. H. W.; Schoenlein, R. W. Picosecond X-ray Absorption Spectroscopy of a Photoinduced Iron(II) Spin Crossover Reaction in Solution. *J. Phys. Chem. A* **2006**, *110*, 38−44.

(43) Hathcock, D. J.; Stone, K.; Madden, J.; Slattery, S. J. Electron Substituent Effects on Reddox and Spin State Properties of Iron(II) Bis-Terpyridyl Complexes. *Inorg. Chim. Acta* **1998**, *282*, 131−135.

(44) Bouzaid, J.; Schultz, M.; Lao, Z.; Bartley, J.; Bostrom, T.; McMurtrie, J. Supramolecular Selection in Molecular Alloy. *Cryst. Growth Des.* **2012**, *12*, 3906−3916.

(45) Burdett, J. J.; Gosztola, D.; Bardeen, C. J. The Dependence of Singlet Exciton Relaxation on Excitation Density and Temperature in Polycrystalline Tetracene Thin Films: Kinetic Evidence for a Dark Intermediate State and Implications for Singlet Fission. *J. Chem. Phys.* **2011**, *135*, 214508.

(46) Chen, L. X.; Zhang, X. Photochemical Processes Revealed by X-ray Transient Absorption Spectroscopy. *J. Phys. Chem. Lett.* **2013**, *4*, 4000−4013.

(47) Smolentsev, G.; Soldatov, A. V. Quantitative Local Structure Refinement from XANES: Multi-Dimensional Interpolation Approach. *J. Synchrotron Radiat.* **2006**, *13*, 19−29.

(48) Smolentsev, G.; Soldatov, A. V. FitIt: New Software to Extract Structural Information on the Basis of XANES Fitting. *Comput. Mater. Sci.* **2007**, *39*, 569−574.

(49) http://www.nano.sfedu.ru/fitit.html.

(50) http://cars9.uchicago.edu/ifeffit/.

(51) Ankudinov, A. L.; Ravel, B.; Rehr, J. J.; Conradson, S. D. Real-Space Multiple-Scattering Calculation and Interpretation of X-ray Absorption Near-Edge Structure. *Phys. Rev. B* **1998**, *58*, 7565−7576.

(52) http://leonardo.phys.washington.edu/feff.

(53) Jun, S.; Lee, J. H.; Kim, J.; Kim, J.; Kim, K. H.; Kong, Q. Y.; Kim, T. K.; Lo Russo, M.; Wulff, M.; Ihee, H. Photochemistry of HgBr$_2$ in Methanol Investigated Using Time-Resolved X-ray Liquidography. *Phys. Chem. Chem. Phys.* **2010**, *12*, 11536−11547.

(54) te Velde, G.; Bickelhaupt, F. M.; Baerends, E. J.; Fonseca Guerra, C.; van Gisbergen, S. J. A.; Snijders, J. G.; Ziegler, T. Chemistry with ADF. *J. Comput. Chem.* **2001**, *22*, 931−967.

(55) http://www.scm.org (accessed: Oct. 10th, 2013)

(56) Hammer, B.; Hansen, L. B.; Nørskov, J. K. Improved Adsorption Energetics within Density-Functional Theory Using Revised Perdew−Burke−Ernzerhof Functionals. *Phys. Rev. B* **1999**, *59*, 7413−7421.

(57) Chong, D. P. Completeness Profiles of One-Electron Basis Sets. *Can. J. Chem.* **1995**, *73*, 79−83.

(58) Van Lenthe, E.; Baerends, E. J. Optimized Slater-Type Basis Sets for the Elements 1−118. *J. Comput. Chem.* **2003**, *24*, 1142−1156.

(59) Klamt, A.; Schüürmann, G. COSMO: A New Approach to Dielectric Screening in Solvents with Explicit Expressions for the Screening Energy and its Gradient. *J. Chem. Soc., Perkin Trans. 2* **1993**, 799−805.

(60) Klamt, A. Conductor-Like Screening Model for Real Solvents: A New Approach to the Quantitative Calculation of Solvation Phenomena. *J. Chem. Phys.* **1995**, *99*, 2224−2235.

(61) Klamt, A.; Jonas, V. Treatment of the Outlying Charge in Continuum Solvation Models. *J. Chem. Phys.* **1996**, *105*, 9972−9981.

(62) Pye, C. C.; Ziegler, T. An Implementation of the Conductor-Like Screening Model of Solvation within the Amsterdam Density Functional Package. *Theor. Chem. Acc.* **1999**, *101*, 396−408.

(63) Baker, A. T.; Goodwin, H. A. Crystal-Structure of Bis(2,2′-6′,2″-terpyridine)iron(II) Bis(perchlorate) Hydrate. *Aust. J. Chem.* **1985**, *38*, 207−214.

(64) Westre, T. E.; Kennepohl, P.; DeWitt, J. G.; Hedman, B.; Hodgson, K. O.; Salomon, E. I. A Multiplet Analysis of the Fe K-Edge 1s → 3d Pre-edge Features of Iron Complexes. *J. Am. Chem. Soc.* **1997**, *119*, 6297−6314.

(65) Briois, V.; Moulin, C. C. D.; Sainctavit, P.; Brouder, C.; Flank, A. M. Full Multiple-Scattering and Crystal-Field Multiplet Calculations Performed on the Spin Transition FeII(phen)(2)(NCS)(2) Complex at the Iron K(2,3) and L(2,3) X-ray Absorption Edges. *J. Am. Chem. Soc.* **1995**, *117*, 1019−1026.

(66) Capano, G.; Penfold, T. J.; Besley, N. A.; Milne, C. J.; Reinhard, M.; Rittmann-Franck, M. H.; Glatzel, P.; Abela, R.; Rothlisberger, U.; Chergui, M.; et al. The Role of Hartree−Fock Exchange in the Simulation of X-ray Absorption Spectra: A Study of Photoexcited [Fe(bpy)(3)](2+). *Chem. Phys. Lett.* **2013**, *580*, 179−184.

(67) Van Kuiken, B. E.; Khalil, M. Simulating Picosecond Iron K-Edge X-ray Absorption Spectra by ab Initio Methods To Study Photoinduced Changes in the Electronic Structure of Fe(II) Spin Crossover Complexes. *J. Phy. Chem. A* **2011**, *115*, 10749−10761.

(68) Hauser, A. Light-Induced Spin Crossover and the High-Spin → Low-Spin Relaxation. *Top. Curr. Chem.* **2004**, *234*, 155−198.

(69) Yoon, Z. S; Chan, Y. T.; Li, S. N.; Newkome, G. R.; Goodson, T. Ultrafast Time-Resolved Spectroscopy of Self-Assembled Cyclic Fe(II)-Bisterpyridine Complexes. *J. Chem. Phys. B* **2010**, *114*, 11731−11736.

(70) Hauser, A. Ligand Field Theoretical Considerations. *Top. Curr. Chem.* **2004**, *233*, 49−58.

(71) Goodwin, H. A. Spin Crossover in Iron(II) Tris(diimine) and Bis(terimine) Systems. *Top. Curr. Chem.* **2004**, *233*, 59−90.

(72) Jorgensen, C. K. Comparative Crystal Fields Studies of Some Ligands and the Lowest Singlet State of Paramagnetic Nickel(II) Complexes. *Acta Chem. Scand.* **1955**, *9*, 1362−1377.

(73) Henke, W.; Reinen, D. Spectroscopical Investigations of Jahn−Teller Effect in Cu2+ Ion in Terpyridin Complexes Cu(terpy)2X₂ [X = NO3−,ClO4−, Br−]. *Z. Anorg. Allg. Chem.* **1977**, *436*, 187−200.

(74) Creutz, C.; Chou, M.; Netzel, T. L.; Okumura, M.; Sutin, N. Lifetimes, Spectra, and Quenching of the Excited-States of Polypyridine Complexes of Iron(II), Ruthenium(II), and Osmium(II). *J. Am. Chem. Soc.* **1980**, *102*, 1309−1319.

(75) Tribollet, J.; Galle, G.; Jonusauskas, G.; Deldicque, D.; Tondusson, M.; Letard, J.-F.; Freysz, E. Transient Absorption Spectroscopy of the Iron(II) [Fe(phen)₃]²⁺ Complex: Study of the Non-Radiative Relaxation of an Isolated Iron(II) Complex. *Chem. Phys. Lett.* **2011**, *513*, 42−47.

(76) Constable, E. C.; Baum, G.; Dyson, R.; van Eldik, R.; Fenske, D.; Kaderli, S.; Morris, D.; Neubrand, A.; Neuburger, M.; Smith, D. R.; Wieghardt, K.; Zehnder, M .; Zuberbuhler, A. D. Control of Iron(II) Spin States in 2,2 ′:6 ′,2 ″-Terpyridine Complexes Through Ligand Substitution. *Chem.—Eur. J.* **1999**, *5*, 498−508.

(77) Brauchli, S. Y.; Constable, E. C.; Harris, K.; Haussinger, D.; Housecroft, C. E.; Rosel, P. J.; Zampese, J. A. Towards Catenanes Using Pi-Stacking Interactions and Their Influence on the Spin-State of a Bis(2,2′:6′,2″-terpyridine) Iron(II) Domain. *Dalton Trans.* **2010**, *39*, 10739−10748.

(78) Constable, E. C.; Davies, J. E.; Phillips, D.; Raithby, P. R. Coordination Chemistry of 5,5″-Disubstituted 2,2′:6′,2″-Terpyridines. *Polyhedron* **1998**, *6*, 2878−2886.

(79) Laine, P.; Gourdon, C. A.; Launay, J.-P. Chemistry of Iron with Dipicolinic Acid. 4. Mixed-Ligand Complexes of Iron(III) and Related Compounds. *Inorg. Chem.* **1995**, *34*, 5156−5165.

(80) Pelascini, F.; Wesolek, M.; Peruch, F.; De Cian, A.; Kyritsakas, N.; Lutz, P. J.; Kress, J. Iron Complexes of Terdentate Nitrogen Ligands: Formation and X-ray Structure of Three New Dicationic Complexes. *Polyhedron* **2004**, *23*, 3193−3199.

(81) Medlycott, E. A.; Hanan, G. S.; Abedin, T. S. M.; Thompson, L. K. The Effect of Steric Hindrance on the Fe(II) Complexes of Triazine-Containing Ligands. *Polyhedron* **2008**, *27*, 493−501.

(82) McMurtrie, J.; Dance, I. Engineering Grids of Metal Complexes: Development of the 2D M(terpy)(2) Embrace Motif in Crystals. *CrystEngComm* **2005**, *7*, 216−229.

(83) Papai, M.; Vanko, G.; de Graaf, C.; Rozgonyi, T. Theoretical Investigation of the Electronic Structure of Fe(II) Complexes at Spin-State Transitions. *J. Chem. Theory Comput.* **2013**, *9*, 509−519.

(84) Bowman, D. N.; Jakubikova, E. Low-Spin versus High-Spin Ground State in Pseudo-Octahedral Iron Complexes. *Inorg. Chem.* **2012**, *51*, 6011−6019.

(85) Lawson Daku, L. M.; Vargas, A.; Hauser, A.; Fouqueau, A.; Casida, M. E. Assessment of Density Functionals for the High-Spin/Low-Spin Energy Difference in the Low-Spin Iron(II) Tris(2,2′-bipyridine) Complex. *ChemPhysChem* **2005**, *6*, 1393−1410.

(86) Rehr, J. J.; Albers, R. C. Theoretical Approaches to X-ray Absorption Fine Structure. *Rev. Mod. Phys.* **2000**, *72*, 621−654.

(87) Huse, N.; Kim, T. K.; Jamula, L.; McCusker, J. K.; deGroot, F. M. F.; Schoenlein, R. W. Photo-Induced Spin-State Conversion in Solvated Transition Metal Complexes Probed via Time-Resolved Soft X-ray Spectroscopy. *J. Am. Chem. Soc.* **2010**, *132*, 6809−6816.

(88) Huse, N.; Cho, H.; Hong, K.; Jamula, L.; deGroot, F. M. F.; Kim, T. K.; McCusker, J. K.; Schoenlein, R. W. Femtosecond Soft X-ray Spectroscopy of Solvated Transition-Metal Complexes: Deciphering the Interplay of Electronic and Structural Dynamics. *J. Phys. Chem. Lett.* **2011**, *2*, 880−884.

(89) Cho, H.; Strader, M. L.; Hong, K.; Jamula, L.; Gullikson, E. M.; Kim, T. K.; deGroot, F. M. F.; McCusker, J. K.; Schoenlein, R. W.; Huse, N. Ligand-Field Symmetry Effects in Fe(II) Polypyridyl Compounds Probed by Transient X-ray Absorption Spectroscopy. *Faraday Discuss.* **2012**, *157*, 463−474.

(90) Bertoni, R.; Lorenc, M.; Tissot, A.; Servol, M.; Boillot, M. L.; Collet, E. Femtosecond Spin-State Photoswitching of Molecular Nanocrystals Evidenced by Optical Spectroscopy. *Angew. Chem., Int. Ed.* **2012**, *51*, 7485−7489.

(91) van der Veen, R. M.; Kwon, O. H.; Tissot, A.; Hauser, A.; Zewail, A. H. Single-Nanoparticle Phase Transitions Visualized by Four-Dimensional Electron Microscopy. *Nat. Chem.* **2013**, *5*, 395−402.

(92) Vanko, G.; Bordage, A.; Glatzel, P.; Gallo, E.; Rovezzi, M.; Gawelda, W.; Galler, A.; Bressler, A.; Doumy, G.; March, A. M.; et al. Spin-State Studies with XES and RIXS: From Static to Ultrafast. *J. Electron Spectrosc. Relat. Phenom.* **2012**, *188*, 166−171.

(93) Lorenc, M.; Hebert, J.; Moisan, N.; Trzop, E.; Servol, M.; Buron-Le Cointe, M.; Cailleau, H.; Boillot, M. L.; Pontecorvo, E.; Wulff, M.; Koshihara, S.; Collet, E. Successive Dynamical Steps of Photoinduced Switching of a Molecular Fe(III) Spin-Crossover Material by Time-Resolved X-Ray Diffraction. *Phys. Rev. Lett.* **2009**, *103*, 028301.

(94) Owens, J. S.; Geisheimer, A. R.; Bokov, A. A.; Ye, Z. G.; Lezhoff, D. B. The Use of Polarizable [AuX2(CN)(2)](−) (X = Br, I) Building Blocks Toward the Formation of Birefringent Coordination Polymers. *Inorg. Chem.* **2010**, *49*, 9609−9616.

(95) Bodenthin, Y.; Pietsch, U.; Mohwald, H.; Kurth, D. G. Inducing Spin Crossover in Metallo-Supramolecular Polyelectrolytes through an Amphiphilic Phase Transition. *J. Am. Chem. Soc.* **2005**, *127*, 3110−3114.

(96) Bodenthin, Y.; Schwarz, G.; Tomkowicz, Z.; Geue, T.; Haase, W.; Pietsch, U.; Kurth, D. G. Liquid Crystalline Phase Transition Induces Spin Crossover in a Polyelectrolyte Amphiphile Complex. *J. Am. Chem. Soc.* **2009**, *131*, 2934−2941.

(97) Schwarz, G.; Bodenthin, Y.; Tomkowicz, Z.; Haase, W.; Geue, T.; Kohlbrecher, J.; Pietsch, U.; Kurth, D. G. Tuning the Structure and the Magnetic Properties of Metallo-Supramolecular Polyelectrolyte−Amphiphile Complexes. *J. Am. Chem. Soc.* **2011**, *133*, 547−558.

(98) Jamula, L. L.; Brown, A. M.; Guo, D.; McCusker, J. K. Synthesis and Characterization of a High-Symmetry Ferrous Polypyridyl Complex: Approaching the ⁵T₂/³T₁ Crossing Point for Feᴵᴵ. *Inorg. Chem.* **2014**, *53*, 15−17.

(99) Dixon, I. M.; Alary, F.; Boggio-Pasqua, M.; Heully, J. L. The (N₄C₂)²⁻ Donor Set as Promising Motif for Bis(tridentate) Iron(II) Photoactive Compounds. *Inorg. Chem.* **2013**, *52*, 13369−13374.

(100) Liu, Y.; Harlang, T.; Canton, S. E.; Chabera, P.; Suarez-Alcantara, K.; Fleckhaus, A.; Vithanage, D. A.; Goransson, E.; Corani, A.; Lomoth, R.; et al. Towards Longer-Lived Metal-to-Ligand Charge Transfer States of Iron(II) Complexes: An N-Heterocyclic Carbene Approach. *Chem. Commun.* **2013**, *49*, 6412−6414.

(101) Boillot, M. L.; Zarembovitch, J.; Sour, A. Ligand-Driven Light-Induced Spin Change (LD-LISC): A Promising Photo Magnetic Effect. *Top. Curr. Chem.* **2004**, *234*, 261−276.

(102) Lawson-Daku, M. L.; Hauser, A. Ab Initio Molecular Dynamics Study of an Aqueous Solution of [Fe(bpy)(3)](Cl)(2) in the Low-Spin and in the High-Spin States. *J. Phys. Chem. Lett.* **2010**, *1*, 1830−1835.

(103) Cammarata, M.; Lorenc, M.; Kim, T. K.; Lee, J. H.; Kong, Q. Y.; Pontecorvo, E.; Lo Russo, M.; Schiro, G.; Cupane, A.; Wulff, M.; Ihee, H. Impulsive Solvent Heating Probed by Picosecond X-ray Diffraction. *J. Chem. Phys.* **2006**, *124*, 124504.

(104) Kjaer, K. S.; van Driel, T. B.; Kehres, J.; Haldrup, K.; Khakhulin, D.; Bechgaard, K.; Cammarata, M.; Wulff, M.; Sorensen, T. J.; Nielsen, M. M. Introducing a Standard Method for Experimental Determination of the Solvent Response in Laser Pump, X-ray Probe Time-Resolved Wide-Angle X-ray Scattering Experiments on Systems in Solution. *Phys. Chem. Chem. Phys.* **2013**, *15*, 15003−15016.

4545

dx.doi.org/10.1021/jp5003963 | *J. Phys. Chem. C* 2014, 118, 4536−4545